

**Nanometer-sized divalent manganese-hydrous silicate domains in geothermal
brine precipitates**

Alain Manceau^{1,*} and Darrell L. Gallup²

¹ Environmental Geochemistry Group, Maison des Géosciences, Univ. J. Fourier, BP 53, 38041
Grenoble Cedex 9, France.

² Unocal Corporation, 1160 N. Dutton Avenue, Ste. 200, Santa Rosa, CA 95401, USA.

Key words: XRD, EXAFS, IR, geothermal scale, Mn-phyllosilicate

Running Title: Nanometer-sized manganese hydrous silicate

* Author to whom correspondence should be addressed. E-mail: Alain.Manceau@ujf-grenoble.fr

ABSTRACT

X-ray diffraction, infrared spectroscopy, and x-ray absorption (XANES and EXAFS) spectroscopy were combined to characterize poorly-crystalline Mn-rich silicate scale deposited from brine at a geothermal field in Indonesia. The precipitate has a vitreous pink-amber appearance, a nearly pure $\text{SiO}_2\text{-MnO-H}_2\text{O}$ chemical composition, and a bulk Mn/Si atomic ratio of 0.63. X-ray microfluorescence indicated that the sample consists of Mn-free and Mn-containing silica domains, whose Mn/Si ratio (1.2 ± 0.4) ranges between those of 2:1 and 1:1 phyllosilicates. The XRD pattern is characterized by a broad scattering band spanning from ~ 6 Å to ~ 2.5 Å with weak modulations at 5.3, 3.5 and 2.72 Å, and a faint band at 1.605 Å. A surrogate was synthesized in an O_2 -free atmosphere by mixing and aging at 150°C for 3 hours a MnCl_2 and a sodium meta-silicate solution. Its XRD pattern was similar to the scale sample, but the two reflections at 2.72 and 1.605 Å were enhanced and the former was asymmetrical as in randomly-stacked layered compounds. Diffraction data are consistent with a mixture of amorphous silica and a poorly ordered manganoo sheet silicate with a domain size of 40-50 Å for the scale and 50-60 Å for the surrogate material. The divalent oxidation state of manganese was confirmed by XANES spectroscopy, and the presumed existence of trioctahedral $[\text{Mn}^{2+}]_3(\text{O},\text{OH})$ clusters having a clay-like local structure was corroborated by the existence of a weak vibration band at 600-650 cm^{-1} by infrared spectroscopy. The connectivity of Mn octahedra was examined using EXAFS spectroscopy by comparing the local structure of Mn in the scale sample and in a large series of Mn compounds having different kinds of Mn octahedra and Si tetrahedra linkages. The manganoo scale has a polyhedral local structure resembling that of sheet silicates, in which metal octahedra are assembled by edges and share corners with ditrigonal SiO_4 rings. Similar short range ordering has been described in iron and aluminum silicate scales, but the manganese silicate scale has a lower domain size owing to the greater misfit between the lateral dimensions

of the Mn and Si sheets. The strain induced by the shrinkage of the Mn sheet to fit the Si sheet(s) is alleviated by the nanometer size of the two-dimensional hydrous silicate domains.

INTRODUCTION

Geothermal energy has been exploited for several decades as a renewable energy source. Both dry steam and hot water reservoirs are used to generate electricity or for space heating. In hydrothermal reservoirs, the water is usually in equilibrium with associated rocks and minerals, resulting in significant dissolved constituents. Total dissolved element concentrations in geothermal brines commonly range from 0.5 to 20 wt. %. When these brines are brought to the surface through wells, the flashpoint of steam is reached. The flashing process decreases the temperature and pressure of the brines, while concentrating the dissolved solids. Consequently, flashing usually results in the supersaturation of some dissolved species followed by their precipitation and deposition as scale on any surfaces with which they come into contact. Scales can plug conduits, heat exchangers, wells, and the subterranean formation in the vicinity of brine disposal wells.

An especially troublesome component of hot brine is silica. Prior to tapping the geothermal resource, the brine is generally saturated with respect to quartz and other silica-bearing minerals. The form of dissolved silica in brine is usually mono-silicic acid, Si(OH)_4 . Because of flashing, the decrease of temperature and the increase of the concentration of Si(OH)_4 often results in exceeding the solubility of silica and leading to the scale deposition of amorphous silica owing to more rapid precipitation than other silica polymorphs; *i.e.*, quartz, cristobalite, and tridymite (Fournier, 1985). Nearly pure amorphous silica may deposit from low salinity brines. However, amorphous silica is often contaminated with metals in higher salinity brines. The most common metal silicate scales encountered in geothermal brine-handling systems are iron and aluminum silicates (Manceau et al., 1995; Gallup, 1998). At a geothermal field in Indonesia, we recently encountered a vitreous pink-amber precipitate in a brine-handling facility. The scale appeared downstream of a flashing vessel where the brine pH was ca. 8.0, the temperature was 152 °C and the pressure was 690 kPa. The scale adhered to piping much more tightly than any previously

observed scale. Chemical analysis revealed that this scale contained 46.9 % SiO_2 and 34.8 % MnO , thereby rendering its pink color. The unusually high Mn content of this scale was of interest. To improve our understanding of metal-silicate scaling mechanisms and the current technology of scale inhibition, we examined the mineralogy of the scale and some related phases.

MATERIALS AND METHODS

Geological Setting and Geochemistry of Hydrothermal Fluids

The hydrothermal field is located in an active volcanic range in Indonesia. The regional stratigraphy begins with a thick Paleozoic metasedimentary sequence, consisting of regionally metamorphosed meta-argillite, quartzite, and marble, which has been intruded in places by a series of granitic Mesozoic plutons. These basement rocks are overlain by Tertiary marine sedimentary rocks. The Tertiary sediments are in turn capped by voluminous Neogene and Quaternary volcanic and volcanoclastic rocks associated with the volcanic arc. Much of the volcanism is andesitic in composition, but the Quaternary arc is characterized by voluminous rhyolitic ash flow tuffs. The silicic volcanism is associated with elevated regional heat flow and crustal uplift. The most recent volcanic unit in the field is a biotite dacite lava with glassy texture and flow banding structure.

The extraction well was drilled to a depth of 1722 m. The well fluid composition is given in Table 1. The reservoir brine pH is estimated to be about 5.5 at 287 °C. Upon production to the surface, flashing of the highly enriched bicarbonate brine causes the pH to increase to 7.5 - 8.5 at 152 °C. Calcite scaling in the production well is nonexistent owing to the low calcium concentration in the brine. Amorphous silica is slightly undersaturated in the wellbore, but flashing to the elevated pH range drives silica deposition together with manganese on surface piping and reinjection brine wellbore pipes. The enrichment of manganese in the brine, compared to most other geothermal systems, is believed to be related to the slightly acidic reservoir fluid

leaching the metal from the sedimentary marine rocks, preferentially to calcium and magnesium. Modeling suggests that manganese occurs in the brine as a bicarbonate complex (Spycher and Reed, 1989). In most geothermal brines, manganese does not precipitate directly with silica. In this unusual geothermal system, however, Mn^{2+} is sufficiently prevalent relative to Mg^{2+} , Ca^{2+} , Fe^{2+} and Al^{3+} to form almost pure Mn-silicate scale.

Description of samples studied

The scale sample is hard and has a vitreous luster. A 30 μm -thick polished thin section was examined by polarizing microscope. The sample is transparent with a 1st order gray birefringence as for silica. However, in contrast to silica, the matrix has a general pink tint, and grains have an acicular shape. The color intensity is inhomogeneous, being more pronounced in millimeter-wide veinlets. An average sample was ground in an agate mortar for infrared (IR), x-ray diffraction (XRD) and extended x-ray absorption fine structure (EXAFS) measurements. Major elements were analyzed by inductively coupled plasma atomic emission spectroscopy (ICP-AES) and trace elements by inductively coupled plasma mass spectroscopy (ICP-MS). Six reference samples were also studied: pyrochroite ($\text{Mn}(\text{OH})_2$), poorly crystalline Mn(II)-phyllosilicate, tephroite (Mn_2SiO_4), pyroxmangite (MnSiO_3), rhodonite (MnSiO_3), and manganpyrosomalite ($(\text{Mn,Fe})_8\text{Si}_6\text{O}_{15}(\text{OH,Cl})_{10}$).

The poorly crystalline Mn(II)-phyllosilicate was prepared as follows: 20 mL of 1.59 M MnCl_2 solution and 300 mL of 0.02 M sodium meta-silicate ($\text{SiO}_2\text{Na}_2\text{O}$) solution were placed into a 1 L Hastelloy C-276 pressure reactor. The Mn:Si mol ratio of the reactants was set at 3:4. The headspace in the reactor was filled with nitrogen to prevent Mn^{2+} oxidation. The reaction mixture was heated to 150 °C with stirring for 3 hours, and the final pH was 10.1. The mixture was removed from the reactor into a glove bag filled with N_2 and through a cooling coil to prevent flashing. Next, the precipitate was filtered through a Whatman #1 (11 μm) paper, washed with

distilled water, and dried overnight under N₂ atmosphere. The synthetic phase was pink in color, indicating that the manganese remained in a reduced state.

Analyses

IR analysis was performed on an ATI / Mattson Research Fourier transform (FT)-IR spectrometer (resolution 5 cm⁻¹). Spectra were recorded in transmission mode on pellets in a KBr matrix. The XRD measurement was performed on a Siemens D5000 diffractometer with Cu K α x-ray radiation wavelength and a Si/Li solid-state detector. The data were collected in step scan mode with a step interval of 0.04° and a counting time of 15 s/point. Mn K-edge x-ray absorption near edge structure (XANES) and powder extended x-ray absorption fine structure (EXAFS) spectra were collected at ambient temperature and in transmission mode on the D42 station at the LURE synchrotron facility at Orsay, France. A Si(331) channel-cut monochromator was used. Gas ionization chambers contained an argon/helium mixture to attenuate the beam intensity by ~20% before and ~50% after the samples. The absolute energy of the spectra was referenced to the first inflection point of elemental Mn (6539 eV).

All XANES spectra were normalized to unit step in the absorption coefficient from below the edge to the middle of the first EXAFS oscillation. Both EXAFS and XANES data were reduced and analyzed using WinXAS (Ressler, 1998). Radial structure functions (RSFs) were obtained by the Fourier transform of k^3 -weighted normalized EXAFS spectra from the reciprocal k space to the distance R space. RSFs were not corrected for EXAFS phase-shifts, causing peaks to appear at shorter distances ($R+\Delta R$, with $\Delta \sim -0.3$ to -0.4 Å) relative to the true near-neighbor distance (R). Each peak in the RSF was then isolated and back-transformed for atomic shell analysis. Partial EXAFS spectra (χ_O , χ_{Mn} and χ_{Si} functions) were fitted by least-squares with theoretical phase shift and amplitude functions calculated *ab initio* with the FEFF 7.02 code (Rehr et al., 1991). Fits were optimized by minimizing the residual parameter Res defined as:

$$Res = \frac{\sum_{i=1}^j |\chi_{\text{exp}}(i) - \chi_{\text{theo}}(i)|}{\sum_{i=1}^j \chi_{\text{exp}}(i)} \cdot 100$$

where j is the number of points in the fit window, and χ_{exp} and χ_{theo} are the experimental and theoretical partial EXAFS functions. The S_0^2 scaling factor was calibrated with pyrochroite for the Mn shell, and with tephroite for the Si shell. From the comparison between EXAFS and crystallographic data of the standards, the absolute accuracy in interatomic distance (R) and coordination number (N) values is typically $\pm 0.03 \text{ \AA}$ and $\pm 30\%$. The relative precision is better.

RESULTS

Chemical composition

The mass concentrations of major elements in the scale sample are $\text{SiO}_2 = 46.9 \%$, $\text{MnO} = 34.8 \%$, $\text{Al}_2\text{O}_3 = 1.6 \%$, $\text{Fe}_2\text{O}_3 = 0.9 \%$, $\text{MgO} = 0.8 \%$, $\text{Na}_2\text{O} = 0.7 \%$, $\text{K}_2\text{O} = 0.6 \%$, $\text{CaO} = 0.4 \%$, $\text{P}_2\text{O}_5 = 0.3 \%$, and the loss on ignition is 13.7% . The sum of all other elements amounts to less than $0.1 \text{ wt. } \%$. In addition to Si and Mn, this sample contains significant structural water/OH ($< \sim 10 \text{ wt. } \%$) in an amount higher than in amorphous silica (Graetsch, 2002). The scale sample is thus a nearly pure $\text{SiO}_2\text{-MnO-H}_2\text{O}$ compound with a bulk Mn/Si atomic ratio (0.63) similar to sepiolite (0.67), and lower than trioctahedral 1:1 (1.5, e.g., serpentine) and 2:1 phyllosilicates (0.75, e.g., talc), and higher than palygorskite (0.5). The homogeneity of Mn in the sample was investigated by X-ray microfluorescence on the 10.3.2 spectrometer of the Advanced Light Source (LBNL, Berkeley). A $4 \times 4 \text{ mm}$ area of the $30 \text{ }\mu\text{m}$ -thick thin section examined by optical microscopy was scanned under a 10 keV X-ray beam at $7 \times 7 \text{ }\mu\text{m}$ resolution, while recording the Mn $K\alpha$ X-ray fluorescence (data not shown). About 50% of the mapped area contained only Si, and in the other half the intensity of the Mn $K\alpha$ line varied by a factor two. Therefore, the actual Mn/Si ratio in the Mn-containing area is about 1.2 ± 0.4 , and ranges between the stoichiometry of 2:1 and 1:1 phyllosilicates. The chemical composition of the synthetic manganoan hydrous

silicate is $\text{SiO}_2 = 45.7\%$, $\text{MnO} = 40.5\%$, $\text{Fe}_2\text{O}_3 = 0.18\%$, $\text{MgO} = 0.10\%$, $\text{Na}_2\text{O} = 2.21\%$, $\text{CaO} = 0.28\%$, and ignition loss = 8.8% . The Mn and Si are in 0.75 ratio, as expected from the composition of the mother solution.

XRD

The XRD pattern of the scale sample is characterized by a prominent broad hump centered at about 3.5 \AA with three weak intensity maxima at 5.3 , 3.5 and 2.72 \AA , and a faint reflection at 1.605 \AA (Fig. 1). The broad scattering feature at $15 - 30^\circ 2\theta$ is attributed to amorphous silica. If present, opal-A is probably very minor because it has a broad and featureless scattering band at 4.1 \AA (Jones and Segnit, 1971). The bands at 2.72 \AA and 1.605 \AA are also observed in the synthetic Mn hydrous silicate. We assume that the two bands arise from the same structural unit in the scale and synthetic compounds. The peak at 1.605 \AA is attributed to the 06-33 reflection and that at 2.72 \AA to the 20-13 reflection of disordered layer silicates (orthogonal layer setting). The asymmetry of the 2.72 \AA peak on its high-angle side is believed to arise from the residual 02 l and 1 l reflections in layer minerals lacking three-dimensional periodicity (Brindley and Brown, 1980). In $\text{Mn}(\text{OH})_2$, the 06-33 and 20-13 reflections (or 110 and 100 in hexagonal layer setting) are at 1.66 and 2.87 \AA . The reduction of the $d(hk0)$ values in the Mn-Si scale is consistent with manganoan hydrous silicate structural units because the lateral dimension of an Mn-rich octahedral sheet in phyllosilicates is reduced to relieve the misfit with the attached tetrahedral sheet(s) (Guggenheim and Eggleton, 1987, 1988). The absence of visible 02-11 band at about $1.605 \times 3 = 4.8\text{ \AA}$ ($18.4^\circ 2\theta$) is explained by the sample composition since the $I(20-13)/I(02-11)$ ratio in c^* -disordered trioctahedral phyllosilicates depends on the chemical composition of the octahedral sheet, and is a maximum for 3d transition elements. For example, in pure Zn-smectites the 02-11 band is about 10 times less intense than the 20-13 band (Decarreau, 1985; Gallup et al., 2003). Consequently, the XRD pattern of the unknown sample provides suggestive evidence for poorly crystalline manganese hydrous silicate domains having a two-dimensional extension. The

full width at half maximum (FWHM) of the 06-33 reflections were used to estimate the particle size using the Debye-Scherrer formula $t = 0.9\lambda/B\cos\theta_B$, where t is the size of the grain (actually the average dimension of coherent scattering domains), λ is the wavelength of x-ray used ($\text{CuK}\alpha = 1.542 \text{ \AA}$) and θ_B is Bragg's angle. B was calculated from the following equation $B = (B_m^2 - B_s^2)^{1/2}$, where B_m is the FWHM of the sample and B_s is the FWHM of a well-crystallized standard used to correct instrumental broadening. Domain sizes obtained for the scale and surrogate materials are 40-50 \AA and 50-60 \AA , respectively. The higher domain size of the laboratory-derived surrogate is consistent with the enhanced intensity of the 06-33 and 20-13 reflections in this sample (Fig. 1). The glassy texture of the scale sample hampered the preparation of oriented aggregates to reinforce the contribution from 00l reflections on the XRD pattern.

IR

The scale and synthetic Mn silicate samples have similar IR patterns with main absorption bands at 3450 (not shown), 1650, 1000, 600-650, and 450 cm^{-1} (Fig. 2). The bands at 3450 and 1650 cm^{-1} are related to water molecules, and the bands at 1000 and 450 cm^{-1} are common to all silicates with tetrahedrally coordinated silicon (Etchepare et al., 1974; Moenke, 1974; Etchepare et al., 1978). Although the two IR spectra present some similarities with that of noncrystalline silica (e.g., opal-A), distinct differences are noted. The prominent Si-O-Si bending band at 1000 cm^{-1} is significantly shifted relative to that of silica minerals ($\sim 1100 \text{ cm}^{-1}$). In silica, only low-cristobalite and opal-C have an absorption band at $\sim 650 \text{ cm}^{-1}$ as observed experimentally here (Etchepare et al., 1978). However, this mineral species assignment is disregarded because no crystalline opal was detected by x-ray diffraction and that cristobalite and opal-C have an intense band at 800 cm^{-1} (Graetsch et al., 1994), which is not present in the scale sample. Instead, striking spectral resemblance is observed with sepiolite (Wollast et al., 1968; Nagata et al., 1974; Yenyol, 1986; Webb and Finlayson, 1987). The $\sim 650 \text{ cm}^{-1}$ band of sepiolite was ascribed to the

[Mg]₃OH deformation modes (Russell et al., 1970). The position of this band is nearly independent of the nature of the octahedral cation (Wilkins and Ito, 1967; Gerard and Herbillon, 1983; Decarreau et al., 1987, 1992), and supports the possible existence of trioctahedral [Mn²⁺]₃OH clusters inferred from XRD data. The IR data also suggest that the hydrous manganese silicate domains have a 2:1 local structure because the intensity ratio of the 650 to 450 cm⁻¹ bands is low in 2:1 clays and high in 1:1 clays (Kermarec et al., 1994).

XANES spectroscopy

The XANES spectra of the scale and synthetic Mn silicate samples are compared to Mn²⁺ (Mn(OH)₂), Mn³⁺ (β-MnOOH), and Mn⁴⁺ (ramsdellite, MnO₂) references in Figure 3. As reported in other studies, the energy of the edge position increases with the formal valence (Bargar et al., 2000; Manceau et al., 2000). The position in energy of the two Mn silicates coincides with that of the Mn²⁺ reference indicating that Mn is divalent. This result is consistent with the pink color of the two samples under transmitted light (Rossman, 1988), and with the assignment of the infrared band at 600-650 cm⁻¹.

EXAFS spectroscopy

The EXAFS patterns of the two Mn silicate samples are obviously similar (Fig. 4a). The multiple wave frequencies and structured shape of the EXAFS spectra contrasts with the essentially featureless nature of the XRD traces, and indicate that the Mn environment involves short range order but long range disorder. In Fourier space (Figure 4b), two intense peaks are shown at low distance (labeled A and B) and weaker, but significant, atomic shell peaks at higher distance (labeled C, D and E). The first peak arises from the oxygen coordination shell about Mn atoms and the second is so intense that it should result (at least partly) from Mn nearest neighbors. Both the height of the first metal shell peak, and the presence of higher distance peaks

in the Fourier transform at $R + \Delta R \sim 4.0, 5.0$ and 6.5 \AA , indicate that the size of the Mn structural entities is at least a few tens of angstroms (Manceau and Calas, 1986).

Usually, the nature of cations located in the immediate vicinity of the probed atom (here Mn) and the connectivity of metal polyhedra are determined by simulating the unknown EXAFS spectrum with plausible atomic pairs (here Mn-Mn and Mn-Si on the basis of chemical analysis) until a satisfactory spectral fit is obtained. As with any fitting technique, there are concerns about the uniqueness of the analysis, especially when the matrix contains light atoms, such as silicon, because of their weak scattering contribution relative to transition metals. In the case of hydrous layer silicates, this difficulty is avoided by polarized EXAFS, but this technique is not applicable here because the material under study is not anisotropic. Therefore, the local structure of the unknown sample was compared to those of a selection of reference compounds. As shown below, the nature of the cations located in the immediate vicinity of Mn atoms could be identified, and the connectivity of Mn and Si polyhedra determined, with a good level of confidence.

Mn(OH)₂-like local structure. One of the simplest divalent Mn compounds is Mn(OH)₂, which consists of Mn(OH)₆ octahedra linked by edges in a two-dimensional framework (Norlund, 1965) (Fig. 5a). RSF peaks for Mn(OH)₂ are assigned by comparison with Co(OH)₂ because the two hydroxides have the same layer structure (O'Day et al., 1994; Manceau et al., 1999). Peak A in Figure 5b arises from the oxygen ligand shell at 2.20 \AA in Mn(OH)₂, peak B from the nearest Mn shell (Mn1) at 3.32 \AA , peak D' from the second-nearest Mn shell (Mn2, 5.75 \AA), and peak E' from the third-nearest Mn shell (Mn3, 6.64 \AA). Peak E', which is located at twice the distance of peak B, is detected in trioctahedral layer structures because of the alignment of Mn-Mn1-Mn3 cations, which amplifies multiple scattering (MS) paths of the photoelectron. Conversely, this MS path is absent in dioctahedral structures owing to the existence of vacancies at the Mn1 position (Mn-□-Mn3) that break the focusing of the electronic waves (Manceau et al., 1998).

Comparing the peak positions and the imaginary parts of the Fourier transforms for the scale sample and Mn(OH)₂ in the $1.0 \text{ \AA} < R + \Delta R < 3.5 \text{ \AA}$ interval, we find that there is a leftward shift

of the unknown (Fig. 5b). This indicates smaller interatomic distances. Spectral simulation yielded Mn-O distances of 2.18 Å ($N_O = 8$, $\sigma = 0.10$ Å, $\Delta E = 2.7$ eV, $Res = 12$) in the scale sample and 2.21 Å ($N_O = 6$, $\sigma = 0.05$ Å, $\Delta E = 3.1$ eV, $Res = 28$) in Mn(OH)₂. The EXAFS Mn-O distance for Mn(OH)₂ is in good agreement with x-ray diffraction (2.20 Å). According to EXAFS theory, the simultaneous shift to lower $R + \Delta R$ values of both the magnitude and imaginary part of the second RSF peak for the Mn scale relative to Mn(OH)₂ indicates that the second shell of the unknown contains the same atom as in the reference (i.e. Mn), and that the interatomic distance is shorter. This interpretation was confirmed by spectral simulation after singling out and back-transforming to k space the two metal shell RSF peaks. A fair spectral simulation ($Res = 22$) of the Mn-Mn1 shell in the scale sample was obtained assuming 4.2 Mn atoms ($\sigma = 0.10$ Å) at 3.27 Å (Fig. 5c, Table 2). From geometrical considerations, this distance is related also to edge-sharing divalent manganese octahedra. This structural model, however, provided only an approximate fit to the partial EXAFS spectrum at $k < 4.5$ Å⁻¹. Because the wave amplitude of light atoms is maximum at low k (Teo, 1986), the spectral mismatch in this region is suppressed ($Res = 13$) by adding a second cationic shell consisting of Si atoms at 3.34 Å (Fig. 5d, Table 2). This possible structural interpretation is supported by the overlay plot of the scale sample and Mn(OH)₂ metal contributions, which shows that the two waves effectively have a differing envelope at low k , suggesting the existence of an additional shell in the scale (Fig. 5e). Still, this structural interpretation is not robust, and additional support for the existence of Mn-Si pairs is provided below. Attempts to simulate the experimental wave function with a manganese shell at about 3.3 Å together with a second oxygen shell at 3.8 to 4.1 Å instead of Mn-Mn + Mn-Si pairs failed. This may be explained by the high disorder of the O2 shell in manganese silicates (Takéuchi et al., 1969; Narita et al., 1977).

The reduction of amplitude of the metal shell peaks B, D and E in the scale sample originates from structural disorder as indicated by the relatively high Debye-Waller value (σ) of the Mn1 shell (0.10 Å). In the spectral simulation, the distribution of distance was modeled by assuming a

Gaussian fit, and the Mn1 shell was best fit by 5 Mn (in the two-shell fit, Table 2) located at an average distance of 3.27 Å with a continuous distribution of 0.10 Å half-width. The distribution of the Mn-Mn1 distances is too small to resolve, and the fit would be insignificantly improved by assuming two discrete Mn-Mn distances (i.e., a bimodal distribution). This contrasts with the analysis of the $\chi_{\text{Mn-Mn1}}$ functions for pyroxmangite and pyrosmalite, because in these minerals a wave beating occurs at $k = 8 - 10 \text{ Å}^{-1}$, and the spectral simulations required two Mn sub-shells separated by $\Delta R = \pi/(2k) = 0.16 - 0.20 \text{ Å}$ (see below). The relatively limited local disorder of the scale sample is consistent with the hypothesis of small ordered trioctahedral Mn domains, because the disorder only arises from border Mn atoms (higher order Mn-Mn correlations at grain boundaries are obviously weakened).

Olivine-like local structure. Now that the presence of edge-sharing Mn-Mn octahedra in the scale sample has been established, the possibility of edge-sharing between Mn octahedra and Si tetrahedra in a manner analogous to olivine is considered next. In addition to tephroite (Mn_2SiO_4), olivine-like polyhedral connectivity occurs in minerals from the humite and leucophoenicite group, whose Mn-rich members include jerrygibbsite ($\text{Mn}_9(\text{SiO}_4)_4(\text{OH})_2$), alleghanyite ($\text{Mn}_5(\text{OH})_2(\text{SiO}_4)_2$), ribbeite ($\text{Mn}_5(\text{OH})_2(\text{SiO}_4)_2$), and leucophoenicite *sensu stricto* ($\text{Mn}_7(\text{SiO}_4)_2\text{SiO}_4(\text{OH})_2$) (Moore, 1970; Freed et al., 1993). A polyhedral diagram of a portion of the structure common to these minerals and the RSF of tephroite are presented in Figure 6a. The Mn-Si distance across the shared edge typically ranges between 2.8 and 2.9 Å, and this atomic pair produces a pronounced peak after the Mn-O peak (Fig. 6b). The second metal-shell peak in the RSF of tephroite corresponds to the admixture of the Mn-Mn_{edge} and Mn-Si_{corner} pairs. The comparison of the RSFs for tephroite and the scale sample demonstrates that the olivine-type of polyhedral association is not present in the scale sample.

Pyroxenoid-like local structure. This mineral group has the same connectivity of polyhedra as in the olivine-type group, but a different topology (Fig. 7a, 8a). Pyroxenoids are single-chain silicates (like pyroxenes) and, hence, differ at the local scale from the olivine-type group by the

relative number of Mn-Si_{edge} to Mn-Si_{corner} linkages. Whereas in the olivine group each Mn octahedron shares on average 1.5 edges with Si tetrahedra, in the pyroxenoid group the average number of Mn-Si_{edge} linkages per Mn octahedron is significantly lower. In rhodonite and pyroxmangite, this number equals 0.6 (Narita et al., 1977; Pinckney and Burnham, 1988). Consequently, the short distance Mn-Si_{edge} peak observed in the tephroite RSF is not apparent on the RSF (Fig. 7b). Accordingly, this shell was neglected during spectral simulations (Table 2). Conversely, the number of Mn-Si_{corner} linkages is higher in pyroxenoids, being equal to 5.0 in rhodonite and 5.4 in pyroxmangite compared to 3.0 in tephroite.

Figures 7b and 8b show that the RSF peaks have a lower amplitude in rhodonite and pyroxmangite than in the Mn scale sample, despite the good crystallinity of the two references. This noteworthy feature results from the considerable scatter of interatomic distances in the two references owing to the band structure of the Mn layer and the strongly kinked nature of the tetrahedral chains. The octahedral bands contain basically two kinds of sites, those on the inside of the bands and those on their edges. The inner octahedra share corners with apical oxygens of a tetrahedral chain, whereas the outer octahedra share edges and corners with tetrahedra because of the lateral jog of the tetrahedral chains. One Mn shell proved sufficient to fit the frequency of the $\chi_{\text{Mn-Mn1}}$ function for rhodonite, but the wave envelope over the entire k range, and specifically for $k < 5 \text{ \AA}^{-1}$, was poorly reproduced, suggesting the contribution of Si atoms (Fig. 7d). Addition of this shell yielded a satisfactory fit, and the EXAFS distances ($R_{\text{Mn-Mn1}} = 3.39 \text{ \AA}$; $R_{\text{Mn-Si1}} = 3.43 \text{ \AA}$) were in good agreement with the average XRD distances ($R_{\text{Mn-Mn1}} = 3.37 \text{ \AA}$; $R_{\text{Mn-Si1}} = 3.39 \text{ \AA}$; Narita et al., 1977) (Fig. 7e). In contrast to rhodonite, a three-shell fit (two Mn-Mn1 and one Mn-Si1 pairs) was necessary to fit the contribution to EXAFS of the nearest cationic shells of pyroxmangite (Table 2, Fig. 8d-e). The addition of a second Mn shell is justified by the rapid damping of the wave amplitude at increasing k value, which can only be explained by the incoherence of the Mn-Mn distances. The wider dispersion of the Mn-Mn distances in pyroxmangite agrees with XRD data because its asymmetric cell contains seven independent Mn

positions compared to five in rhodonite. The comparison of the $\chi_{\text{Mn-Me}}$ functions for the Mn scale, $\text{Mn}(\text{OH})_2$, rhodonite, and pyroxmangite indicates that the structural order in the unknown is intermediate between $\text{Mn}(\text{OH})_2$ and pyroxenoids, and not distinctive of pyroxenoids.

Hydrous silicate-like local structure. The hydrous manganese silicate reference is manganpyrosmalite $((\text{Mn},\text{Fe})_8\text{Si}_6\text{O}_{15}(\text{OH},\text{Cl})_{10}$; Takéuchi et al., 1969). This mineral has octahedral sheets of manganese joined together by tetrahedral Si sheets whose six-membered rings point alternatively in opposing directions (Fig. 9). The tilting of tetrahedra results from the difference in the lateral dimensions of the Mn and the Si sheets. Besides manganpyrosmalite, the structure of another modulated Mn layer silicate has been refined, bementite $(\text{Mn}_7\text{Si}_6\text{O}_{15}(\text{OH})_8)$ (Heinrich et al., 1994). The two minerals differ essentially by the size of rings of SiO_4 tetrahedra, being twelve-, six-, and four-membered in pyrosmalite, and seven-, six-, and five-membered in bementite. Manganese has a similar local structure in the two modulated Mn layer silicates and, therefore, manganpyrosmalite can be considered to be representative of this group of minerals.

The overlay plot of the RSFs for the scale sample and manganpyrosmalite presented in Fig. 10a reveals interesting similarities in the two structures. The two structures clearly possess the same type of metal shells, with all the Mn-(Mn,Si) distances being shrunk in the unknown as indicated by the leftward shift of the magnitude and imaginary part of peaks B, C, D and E. Peak B in the reference is broadened towards higher $R+\Delta R$ values, and this feature resulted in a wave beating at 10 \AA^{-1} in the k space (Fig. 10b). This node was correctly reproduced by assuming a first subshell of 4.2 Mn atoms at 3.27 \AA and a second of 4.8 Mn at 3.43 \AA (Fig. 10c). As expected from crystallography (Table 2), this structural model provided an approximate fit to the χ function at low k , and the addition of a Si1 shell at 3.44 \AA yielded good spectral agreement over the whole k range (Fig. 10d). The fact that the χ function of the unknown and the reference have the same wave amplitude and envelope at $k < 6 \text{ \AA}^{-1}$ suggests that they have a similar Mn-Si contribution (Fig. 10b). So far, the argument in support of the Si shell has been only moderately compelling because in layer metal silicates the contribution of the nearest Si shell is weak and almost

completely masked by the predominant metal shell contribution across octahedral edges. Strong support for the existence of Mn octahedra – Si tetrahedra corner linkages in the unknown sample comes from the analysis of peak C. In manganpyrosmalite this peak arises from the next-nearest Si shell only, because the second Mn shell (peak D) is at 5.7 – 5.9 Å. The higher oxygen shells are weak scatterers and too disordered to contribute to peak C. In the unknown, peak C is left-shifted to slightly shorter distance. The fact that both the magnitude and the imaginary part of the Fourier transform are translated simultaneously by the same amount means that this peak also arises from silicon in the unknown. Furthermore, the reduction in distance of the Si₂ shell in the Mn scale sample is consistent with the observed shortening of all the Mn – Mn distances as attested by the displacement towards lower $R + \Delta R$ values of peaks B, D and E in comparison to manganpyrosmalite.

EVIDENCE FOR MN HYDROUS SILICATE DOMAINS IN THE SCALE PRECIPITATE

IR spectroscopy shows a weak peak at 600–650 cm⁻¹, which was assigned to the Mn-OH vibration in layer silicate structure by comparison with the IR spectra of phyllosilicates. Thus, this peak in the IR spectrum of the scale sample indicates that manganese atoms are directly bonded to hydroxyls and have a phyllosilicate-like short-range structural order. This interpretation is consistent with chemical analysis and X-ray microfluorescence data, which showed that the Mn/Si atomic ratio of the manganoan area (1.2 ± 0.4) compares closely to those of 2:1 and 1:1 phyllosilicates. The screening by EXAFS spectroscopy of the local structure of Mn in different families of Mn silicates showed that in the unknown sample Mn octahedra are associated by edge and linked to SiO₄ tetrahedra by corners as in hydrous silicates. Therefore, Mn atoms are not present as individual interstitial ions in the siliceous scale matrix, but are segregated in locally ordered domains of sufficient size and abundance to be evident by x-ray diffraction. This latter technique revealed that the scale precipitate contains nanometer-sized two-

dimensional structural units, whose a and b parameters ($a = 5.44$; $b = 9.63$ Å in orthogonal setting) are consistent with sheet silicates. Hazen and Wones (1972) studied the limit of strain of 2:1 trioctahedral phyllosilicates induced by the inherent differences in the lateral dimensions of the tetrahedral and octahedral sheets. For a pure silicon tetrahedral sheet, they found that homogeneous sheet silicates could not be synthesized with divalent metal cations having ionic radii greater than 0.70 – 0.72 Å. Since Mn^{2+} is bigger (0.82 Å), the lateral mismatch between the octahedral and tetrahedral sheets is alleviated in all the Mn silicate reference considered (rhodonite, pyroxmangite and manganpyrosmalite), and also in the 1:1 Mn phyllosilicate caryopilite (Guggenheim and Eggleton, 1998), by inverting certain tetrahedra and rebonding the apices in different ribbon-like and ring-like patterns. The local structure of the Mn hydrous silicate domains possibly differs from those of the crystalline references in having continuous siloxane sheets over a few tens of angstroms. This interpretation is supported by the overall similarity of the short range ordering of Mn in the scale sample and in manganpyrosmalite, which has isolated six-membered SiO_4 rings on each side of the Mn layer. The major structural difference detected by EXAFS between these two compounds lies in the shortening of the Mn-Mn1, Mn-Mn2, Mn-Mn3 and Mn-Si2 interatomic distances in the scale sample. This reduction means that the lateral size of the Mn layer is smaller, as is the case when an (oxyhydr)oxide layer is overlain by one or two continuous tetrahedral SiO_4 sheets like in regular 1:1 and 2:1 phyllosilicates. The strain induced by the shrinkage of the $\text{Mn}(\text{O},\text{OH})_2$ layer would be alleviated then by the small size of the Mn hydrous silicate domains. In other words, although pure large crystals of manganese phyllosilicate are unstable, nanometer-sized layers of this compound may be stabilized by reacting divalent manganese and silica at medium temperature and pressure (152 °C and 690 kPa) in the laboratory and in the field during brine flashing. Also, the somewhat alkaline pH of the brine upon the scale precipitation is consistent with the formation of clay-like manganese domains since a large body of work showed that phyllosilicates readily form upon

reacting aqueous metal with sodium silicate solution or silica in basic condition (Decarreau, 1985; Clause et al., 1992; Badiei and Bonneviot, 1998; Manceau et al., 1999; Gallup et al., 2003).

ACKNOWLEDGMENTS

The authors thank Drs. A. Decarreau and S. Guggenheim for their scientific and editorial comments.

REFERENCES

- Badiei, A.R. and Bonneviot, L. (1998) Modification of mesoporous silica by direct template ion exchange using cobalt complexes. *Inorganic Chemistry*, 37, 4142-4145.
- Bailey, S.W. (1988) *Hydrous phyllosilicates*. 725 p. Mineralogical Society of America, Washington DC.
- Bargar, J.R., Tebo, B.M., and Villinski, J.E. (2000) In situ characterization of Mn(II) oxidation by spores of the marine *Bacillus* sp. strain SG-1. *Geochimica et Cosmochimica Acta*, 64, 2775-2778.
- Brindley, G.W. and Brown, G. (1980) *Crystal structures of clay minerals and their X-ray identification*. 495 p. Mineralogical Society, London.
- Clause, O., Kermarec, M., Bonneviot, L., Villain, F., and Che, M. (1992) Nickel(II) ion-support interactions as a function of preparation method of silica-supported nickel materials. *Journal of the American Chemical Society*, 114, 4709-4717.
- Decarreau, A. (1985) Partitioning of divalent transition elements between octahedral sheets of trioctahedral smectites and water. *Geochimica et Cosmochimica Acta*, 49, 1537-1544.
- Decarreau, A., Colin, F., Herbillon, A., Manceau, A., Nahon, D., Paquet, H., and Trauth-Badaud, D. (1987) Domains segregation in Ni-Fe-Mg bearing smectites. *Clays and Clay Minerals*, 35, 1-10.
- Decarreau, A., Grauby, O., and Petit, S. (1992) The actual distribution of octahedral cations in 2:1 clay minerals : results from clay synthesis. *Applied Clay Science*, 7, 147-167.
- Etchepare, J., Merian, M., and Smetankine, L. (1974) Vibrational normal modes of SiO₂. I. α and β quartz. *Journal of Chemical Physics*, 60, 1873-1876.
- Etchepare, J., Merian, M., and Kaplan, P. (1978) Vibrational normal modes of SiO₂. II. Cristobalite and tridymite. *Journal of Chemical Physics*, 68, 1531-1537.

- Fournier, R.O. (1985) The behavior of silica in hydrothermal solutions. *Reviews in Economic Geology*, 2, 45-61.
- Freed, R.L., Rouse, R.C., and Peacor, D.R. (1993) Ribbeite, a second example of edge-sharing silicate tetrahedra in the leucophoenicite group. *American Mineralogist*, 78, 190-194.
- Fujino, K., Sasaki, S., Takéuchi, Y., and Sadanaga, R. (1981) X-ray determination of electron distributions in forsterite, fayalite and tephroite. *Acta Crystallographica, B* 37, 513-518.
- Gallup, D.L. (1998) Aluminum silicate scale formation and inhibition (2); scale solubilities and laboratory and field inhibition tests. *Geothermics*, 27, 485-501.
- Gallup, D.L., Sugiaman, F., Capuno, V., and Manceau, A. (2003) Laboratory investigation of silica removal from geothermal brines to control silica scaling and produce usable silicates. *Applied Geochemistry*, 18, 1597-1612.
- Gerard, P. and Herbillon, A.J. (1983) Infrared studies of Ni-bearing clay minerals of the kerolite-pimelite series. *Clays and Clay Minerals*, 31, 143-151.
- Guggenheim, S. and Eggleton, R.A. (1987) Modulated 2:1 layer silicates: Review, systematics and predictions. *American Mineralogist*, 72, 726-740.
- Guggenheim, S. and Eggleton, R.A. (1988) Crystal chemistry, classification, and identification of modulated layer silicates. In G.W. Bailey, Ed. *Hydrous phyllosilicates exclusive of the micas*, 19, p. 675-725. Mineralogical Society of America *Reviews in Mineralogy*.
- Guggenheim, S. and Eggleton, R.A. (1998) The crystal structures of greenalite and caryopilite: A system with long-range, in-plane structural disorder in the tetrahedral sheet. *Canadian Mineralogist*, 36, 163-179.
- Graetsch, H., Gies, H., and Topalovic, I. (1994) NMR, XRD and IR study on microcrystalline opals. *Physics and Chemistry of Minerals*, 21, 166-175.
- Graetsch, H. (2002) Structural characteristics of opaline and microcrystalline opal materials. In P.J. Heaney, and C.T. Prewitt, Eds. *Silica. Physical behavior, geochemistry, and materials applications*, 29, p. 209-232. Mineralogical Society of America, Washington, DC.

- Hazen, R.M. and Wones, D.R. (1972) The effect of cation substitutions on the physical properties of trioctahedral micas. *American Mineralogist*, 57, 103-109.
- Heinrich, A.R., Eggleton, R.A., and Guggenheim, S. (1994) Structure and polytypism of bementite, a modulated layer silicate. *American Mineralogist*, 79, 91-106.
- Jones, J.B. and Segnit, E.R. (1971) The nature of opal. I. Nomenclature and constituent phases. *Journal of the Geological Society of Australia*, 18, 57-68.
- Kermarec, M., Carriat, J.Y., Burattin, P., Che, M., and Decarreau, A. (1994) FTIR identification of the supported phases produced in the preparation of silica-supported nickel catalysts. *Journal of Physical Chemistry*, 98, 12007-12017.
- Manceau, A. and Calas, G. (1986) Ni-bearing clay minerals. 2. X-ray absorption study of Ni-Mg distribution. *Clay Minerals*, 21, 341-360.
- Manceau, A., Gallup, D., Ildefonse, P., Hazemann, J.L., and Flank, A.M. (1995) Crystal chemistry of hydrous iron silicate scales deposits at the Salton Sea Geothermal field. *Clays and Clay Minerals*, 43, 304-317.
- Manceau, A., Chateigner, D., and Gates, W.P. (1998) Polarized EXAFS, distance-valence least-squares modeling (DVLS) and quantitative texture analysis approaches to the structural refinement of Garfield nontronite. *Physics and Chemistry of Minerals*, 25, 347-365.
- Manceau, A., Schlegel, M., Nagy, K.L., and Charlet, L. (1999) Evidence for the formation of trioctahedral clay upon sorption of Co^{2+} on quartz. *Journal of Colloid and Interface Science*, 220, 181-197.
- Manceau, A., Schlegel, M.L., Musso, M., Sole, V.A., Gauthier, C., Petit, P.E., and Trolard, F. (2000) Crystal chemistry of trace elements in natural and synthetic goethite. *Geochimica et Cosmochimica Acta*, 64, 3643-3661.
- Moenke, H.H.W. (1974) Silica, the three dimensional silicates, borosilicates and beryllium silicates. In V.C. Farmer, Ed. *The infrared spectra of minerals*, 4, p. 365-382. Mineralogical Society Monograph, London.

- Moore, P.B. (1970) Edge-sharing silicate tetrahedra in the crystal structure of leucophoenicite. *American Mineralogist*, 55, 1146-1165.
- Nagata, H., Shimoda, S., and Sudo, T. (1974) On dehydration of bound water of sepiolite. *Clays and Clay Minerals*, 22, 285-293.
- Narita, H., Koto, K., and Morimoto, N. (1977) The crystal structures of MnSiO_3 polymorphs (rhodonite- and pyroxmangite-type). *Mineralogical Journal*, 8, 329-342.
- Norlund, C.A. (1965) A single crystal x-ray diffraction study of $\text{Mn}(\text{OH})_2$. *Acta Chemica Scandinavica*, 1765-1788.
- O'Day, P.A., Rehr, J.J., Zabinsky, S.I., and Brown, G.E., Jr. (1994) Extended x-ray absorption fine structure (EXAFS) analysis of disorder and multiple-scattering in complex crystalline solids. *Journal of the American Chemical Society*, 116, 2938-2949.
- Pinckney, L.R. and Burnham, C.W. (1988) Effects of compositional variation on the crystal structures of pyroxmangite and rhodonite. *American Mineralogist*, 73, 798-808.
- Rehr, J.J., Mustre de Leon, J., Zabinsky, S.I., and Albers, R.C. (1991) Theoretical X-ray Absorption Fine Structure Standards. *Journal of the American Chemical Society*, 113, 5135-5145.
- Ressler, T. (1998) WinXAS: a Program for X-ray Absorption Spectroscopy Data Analysis under MS-Windows. *Journal of Synchrotron Radiation*, 5, 118-122.
- Rossmann, G.R. (1988) Optical spectroscopy. In F.C. Hawthorne, Ed. *Spectroscopic methods in mineralogy and geology*, 18, p. 207-254. Mineralogical Society of America, Washington DC.
- Russell, J.D., Farmer, V.C., and Velde, B. (1970) Replacement of OH by OD in layer silicates and identification of the vibrations of these groups in infrared spectra. *Mineralogical Magazine*, 37, 869-979.
- Spycher, N.F. and Reed, M.H. (1989) Evolution of a Broadlands-type epithermal ore fluid along alternative P-T paths: implications for the transport and deposition of base, precious and volatile metals. *Economic Geology*, 84, 328-359.

- Takéuchi, Y., Kawada, I., Irimaziri, S., and Sadanaga, R. (1969) The crystal structure and polytypism of manganpyrosmalite. *Mineralogical Journal*, 5, 450-467.
- Teo, B.K. (1986) EXAFS: basic principles and data analysis. 349 p. Springer-Verlag, Berlin.
- Webb, J.A. and Finlayson, B.L. (1987) Incorporation of Al, Mg, and water in opal-A: Evidence from speleotherms. *American Mineralogist*, 72, 1204-1210.
- Wilkins, R.W.T. and Ito, J. (1967) Infrared spectra of some synthetic talcs. *American Mineralogist*, 52, 1649-1661.
- Wollast, R., Mackenzie, F.T., and Bricker, O.P. (1968) Experimental precipitation and genesis of sepiolite at earth-surface conditions. *American Mineralogist*, 53, 1645-1662.
- Yeniyol, M. (1986) Vein-like sepiolite occurrence as a replacement of magnesite in Konya, Turkey. *Clays and Clay Minerals*, 34, 353-356.

Figure Caption

Fig. 1 Experimental powder x-ray diffraction pattern of the scale sample (black line) and the synthetic divalent Mn hydrous silicate (greyed line).

Fig. 2 Infrared spectrum of the scale sample (solid line) and the synthetic divalent Mn hydrous silicate (dotted line).

Fig. 3 Mn K-edge XANES spectra of the scale sample and the synthetic divalent Mn hydrous silicate together with Mn^{2+} ($\text{Mn}(\text{OH})_2$), Mn^{3+} ($\beta\text{-MnOOH}$), and Mn^{4+} (ramsdellite, MnO_2) references.

Fig. 4 Mn K-edge EXAFS spectra (a) and Fourier transforms (b) of the scale sample and the synthetic divalent Mn hydrous silicate. In b), the envelope curve is the magnitude of the complex Fourier transform $((R^2 + I^2)^{1/2})$ and the oscillatory curve is the imaginary part of the transform. The peak positions are not corrected for phase shift and, consequently, are shifted by $\Delta R \sim -0.3$ to -0.4 Å relative to crystallographic R distances.

Fig. 5 a) Polyhedral sketch of the structure of $\text{Mn}(\text{OH})_2$ and projection of the structure onto the ab plane with representation of the Mn-Mn1, Mn-Mn2 and Mn-Mn3 pairs and illustration of the Mn-Mn1-Mn3 focusing effect. b) Fourier transforms of the Mn-EXAFS spectra for the scale sample and $\text{Mn}(\text{OH})_2$. Peak A corresponds to the Mn-O pair, peak B to the Mn-Mn1 pair, peak D' to the Mn-Mn2 pair, and peak E' to the Mn-Mn3 pair. The amplitude of peak E' is enhanced by the alignment of Mn, Mn1, and Mn3 (multiple scattering path of the photoelectron). c) One-shell fit of the electronic wave from peak B for the scale sample assuming $N_{\text{Mn1}} = 4.2$, $\sigma = 0.10$ Å, and $R_{\text{Mn1}} = 3.27$ Å. d) Two-shell fit assuming $N_{\text{Mn1}} = 5.0$, $\sigma = 0.10$ Å, $R_{\text{Mn1}} = 3.27$ Å, $N_{\text{Si1}} =$

3.8, $\sigma = 0.10$ Å, $R_{\text{Si}} = 3.34$ Å. The $R + \Delta R$ window for the inverse Fourier transform is [2.5 - 3.6] Å. e) Fourier filtered contributions to EXAFS of the nearest cationic shells for the scale sample and $\text{Mn}(\text{OH})_2$.

Fig. 6 a) Polyhedral sketch of a portion of the structure common to mineral species from the olivine-, humite-, and leucophoenicite-group of minerals. SiO_4 tetrahedra (dark grey) are linked by edges and corners to MnO_6 octahedra (light grey). After Fujino et al. (1981). b) Comparison of the Fourier transforms for the scale sample and tephroite.

Fig. 7 a) Polyhedral representations of the rhodonite (MnSiO_3) structure showing the layer structure (upper sketch) and the MnO_6 ribbons (light grey) and the kinked SiO_4 single chains (dark grey, lower sketch). After Narita et al. (1977). In rhodonite the periodicity of the SiO_4 , pyroxene-like, single-chains is 5. The octahedral Mn bands of manganoan pyroxenoids contain two different kinds of sites, those on the inside of the bands and those on their edges. The inner octahedra share corners with SiO_4 tetrahedra, whereas the Mn octahedra on the edges of the bands share edges and corners with SiO_4 tetrahedra. The various coordinations of the Mn octahedra result in a considerable scatter of interatomic distances. b) Comparison of the Fourier transforms for the scale sample and rhodonite. c) Fourier filtered contributions to EXAFS of the nearest cationic shells for the scale sample and rhodonite. (d) One-shell fit for rhodonite assuming $N_{\text{MnI}} = 3.4$, $\sigma = 0.10$ Å, and $R_{\text{MnI}} = 3.38$ Å. (e) Two-shell fit for rhodonite assuming $N_{\text{MnI}} = 4.9$, $\sigma = 0.09$ Å, $R_{\text{MnI}} = 3.39$ Å, $N_{\text{SiI}} = 5.3$, $\sigma = 0.09$ Å, $R_{\text{SiI}} = 3.43$ Å. The $R + \Delta R$ window for the inverse Fourier transform is [2.7 - 3.6] Å.

Fig. 8 a) Polyhedral representations of the pyroxmangite (MnSiO_3) structure showing the layer structure (upper sketch), and the MnO_6 ribbons (light grey) and the kinked SiO_4 single chains (dark grey, lower sketch). In pyroxmangite the periodicity of the SiO_4 , pyroxene-like, single-

chains is 7. After Narita et al. (1977). b) Comparison of the Fourier transforms for the scale sample and pyroxmangite. c) Fourier filtered contributions to EXAFS of the nearest cationic shells for the scale sample and pyroxmangite. (d) Two-shell fit for pyroxmangite assuming $N_{\text{Mn1a}} = 7.4$, $\sigma = 0.14 \text{ \AA}$, and $R_{\text{Mn1a}} = 3.21 \text{ \AA}$, $N_{\text{Mn1b}} = 5.4$, $\sigma = 0.14 \text{ \AA}$, and $R_{\text{Mn1a}} = 3.41 \text{ \AA}$. (e) Three-shell fit for pyroxmangite assuming $N_{\text{Mn1a}} = 2.6$, $\sigma = 0.11 \text{ \AA}$, and $R_{\text{Mn1a}} = 3.18 \text{ \AA}$, $N_{\text{Mn1b}} = 5.0$, $\sigma = 0.11 \text{ \AA}$, $R_{\text{Mn1a}} = 3.40 \text{ \AA}$, $N_{\text{Si1}} = 6.4$, $\sigma = 0.11 \text{ \AA}$, $R_{\text{Si}} = 3.42 \text{ \AA}$. The $R + \Delta R$ window for the inverse Fourier transform is $[2.3 - 3.5] \text{ \AA}$.

Fig. 9 Polyhedral representations of the manganpyrosmalite $((\text{Mn,Fe})_8\text{Si}_6\text{O}_{15}(\text{OH,Cl})_{10})$ structure showing the layer structure (upper sketch) and the planar structure (middle and lower sketch). In a same silicate sheet, SiO_4 tetrahedra (dark grey) are turned upside down, yielding a modulated structure. In the middle sketch, only SiO_4 tetrahedra pointing downwards the Mn layer (light grey) are represented, whereas in the lower sketch all octahedra of the silicate sheet are drawn. After Takéuchi et al. (1969).

Fig. 10a) Comparison of the Fourier transforms for the scale sample and manganpyrosmalite. b) Fourier filtered contributions to EXAFS of the nearest cationic shells for the scale sample and manganpyrosmalite. (c) Two-shell fit for manganpyrosmalite assuming $N_{\text{Mn1a}} = 4.2$, $\sigma = 0.07 \text{ \AA}$, and $R_{\text{Mn1a}} = 3.27 \text{ \AA}$, $N_{\text{Mn1b}} = 4.8$, $\sigma = 0.07 \text{ \AA}$, and $R_{\text{Mn1a}} = 3.43 \text{ \AA}$. (d) Three-shell fit for manganpyrosmalite assuming $N_{\text{Mn1a}} = 2.6$, $\sigma = 0.04 \text{ \AA}$, and $R_{\text{Mn1a}} = 3.25 \text{ \AA}$, $N_{\text{Mn1b}} = 5.6$, $\sigma = 0.04 \text{ \AA}$, $R_{\text{Mn1a}} = 3.42 \text{ \AA}$, $N_{\text{Si1}} = 4.2$, $\sigma = 0.04 \text{ \AA}$, $R_{\text{Si}} = 3.44 \text{ \AA}$. The $R + \Delta R$ window for the inverse Fourier transform is $[2.4 - 3.7] \text{ \AA}$.

TABLE 1. Brine composition (mg/kg)

Li	B	HCO ₃ ⁻	F	Na	Mg	Al	SiO ₂	SO ₄ ²⁻	Cl	K	Ca	Mn	Fe	Total dissolved solid
5.4	15	260	3	359	0.5	<0.1	735	162	466	81	2.4	21	0.1	2150

TABLE 2. EXAFS parameters for Mn and Si shells

Sample		Mn-Mn			Mn-Mn			Mn-Si			ΔE	Res
		R (Å)	N	σ (Å)	R (Å)	N	σ (Å)	R (Å)	N	σ (Å)		
Mn(OH) ₂		3.34	6.0 ¹	0.06	-	-	-	-	-	-	6.7	6
Mn scale	One-shell fit	3.27	4.2	0.10	-	-	-	-	-	-	5.2	22
	Two-shell fit	3.27	5.0	0.10 ²	-	-	-	3.34	3.8	0.10 ²	2.0	13
Rhodonite	One-shell fit	3.38	3.4	0.10	-	-	-	-	-	-	6.1	33
	Two-shell fit	3.39	4.9	0.09	-	-	-	3.43	5.3	0.09	0.8	15
	Average XRD value ³	3.37	4.6	-	-	-	-	3.39 ⁴	5.0	-	-	-
Pyroxmangite	Two-shell fit	3.21	7.4	0.14 ²	3.41	5.4	0.14 ²				5.9	23
	Three-shell fit	3.18	2.6	0.11 ²	3.40	5.0	0.11 ²	3.42	6.4	0.11 ²	0.8	15
	Average XRD value ³	3.31	4.6	-	-	-	-	3.41 ⁵	5.4	-	-	-
Pyrosmalite	Two-shell fit	3.27	4.2	0.07 ²	3.43	4.8	0.07 ²				5.4	20
	Three-shell fit	3.25	2.6	0.04 ²	3.42	5.6	0.04 ²	3.44	4.2	0.04 ²	2.1	8
	Average XRD value ⁶	3.37	6.0	-	-	-	-	3.40	2.7	-	-	-

Notes.

1- Held fixed to the crystallographic value.

2- Constrained to be identical for all subshells.

3- After Narita et al. (1977)

4- $R(\text{Mn-Si})_{\text{edge}} = 2.97 \text{ \AA}$, $N(\text{Mn-Si})_{\text{edge}} = 0.6$

5- $R(\text{Mn-Si})_{\text{edge}} = 2.95 \text{ \AA}$, $N(\text{Mn-Si})_{\text{edge}} = 0.6$

6- After Takéuchi et al. (1969)

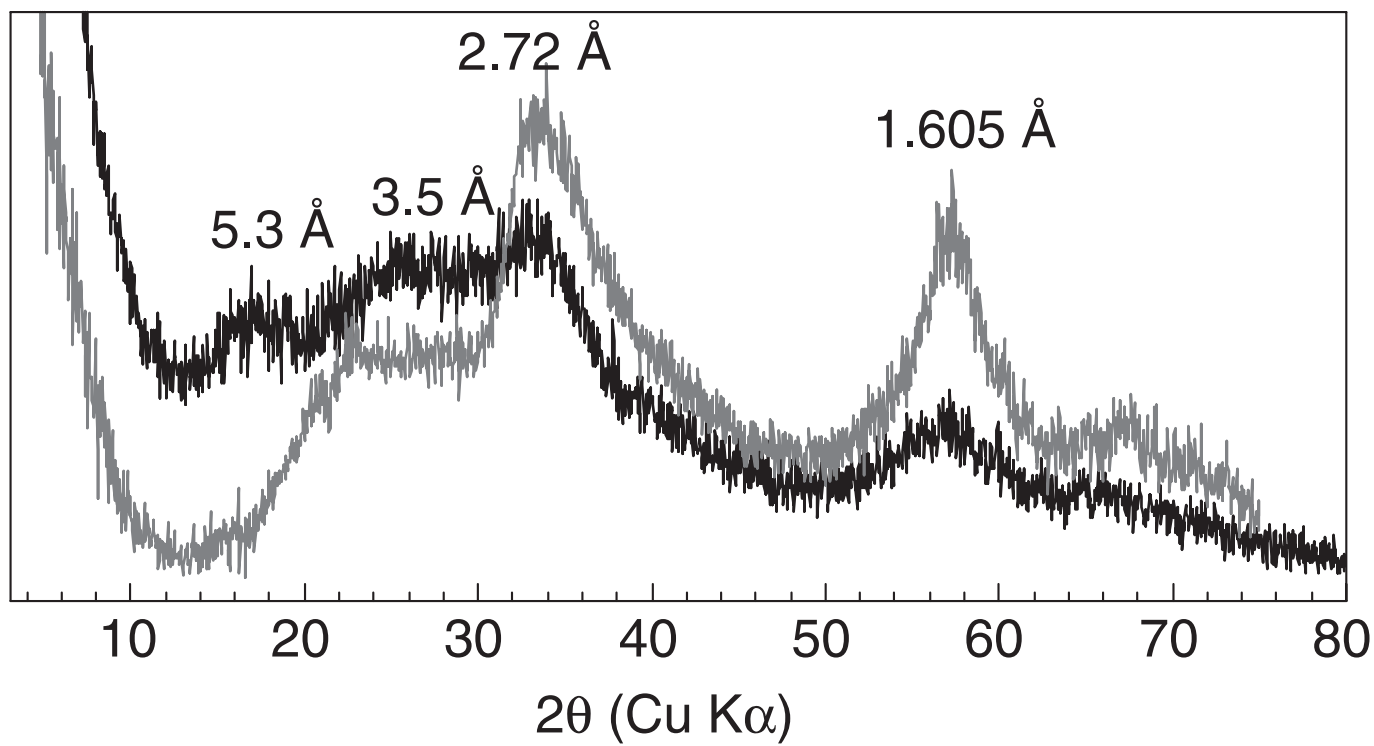


Fig. 1 Manceau and Gallup

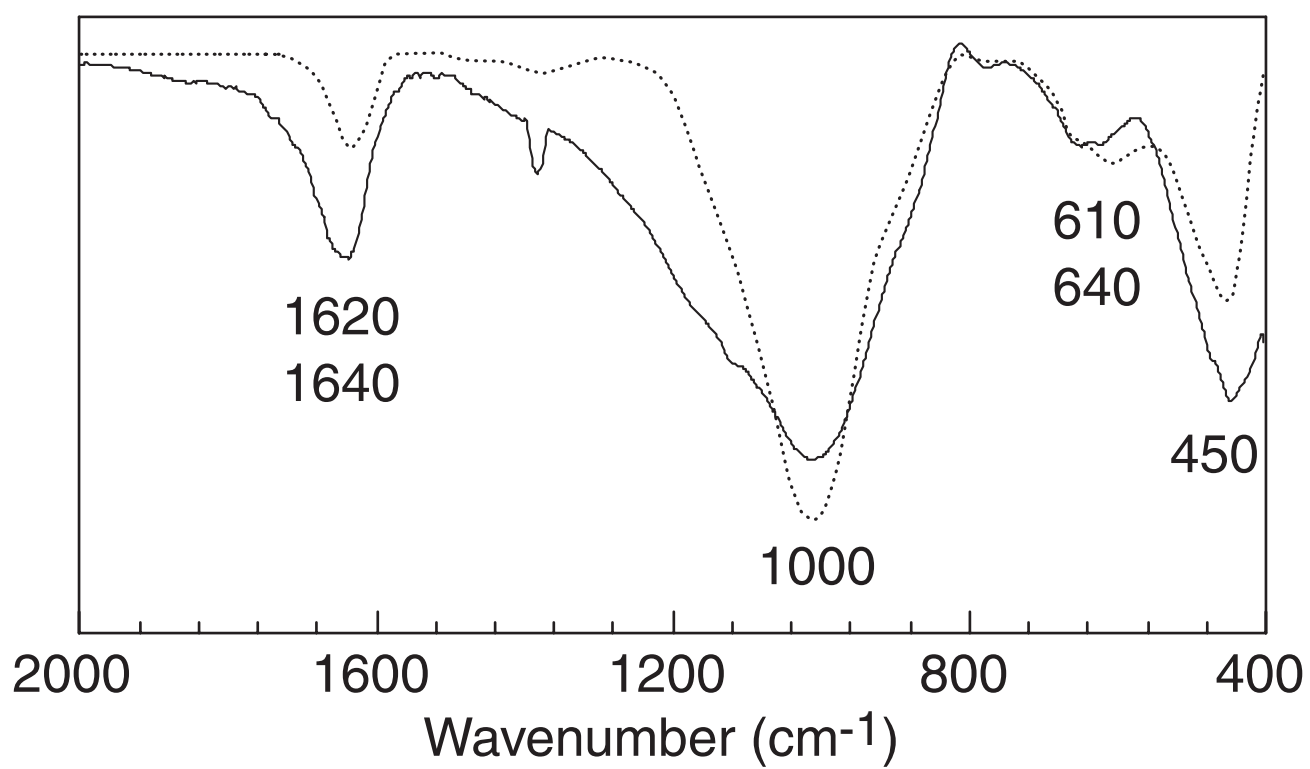


Fig. 2 Manceau and Gallup

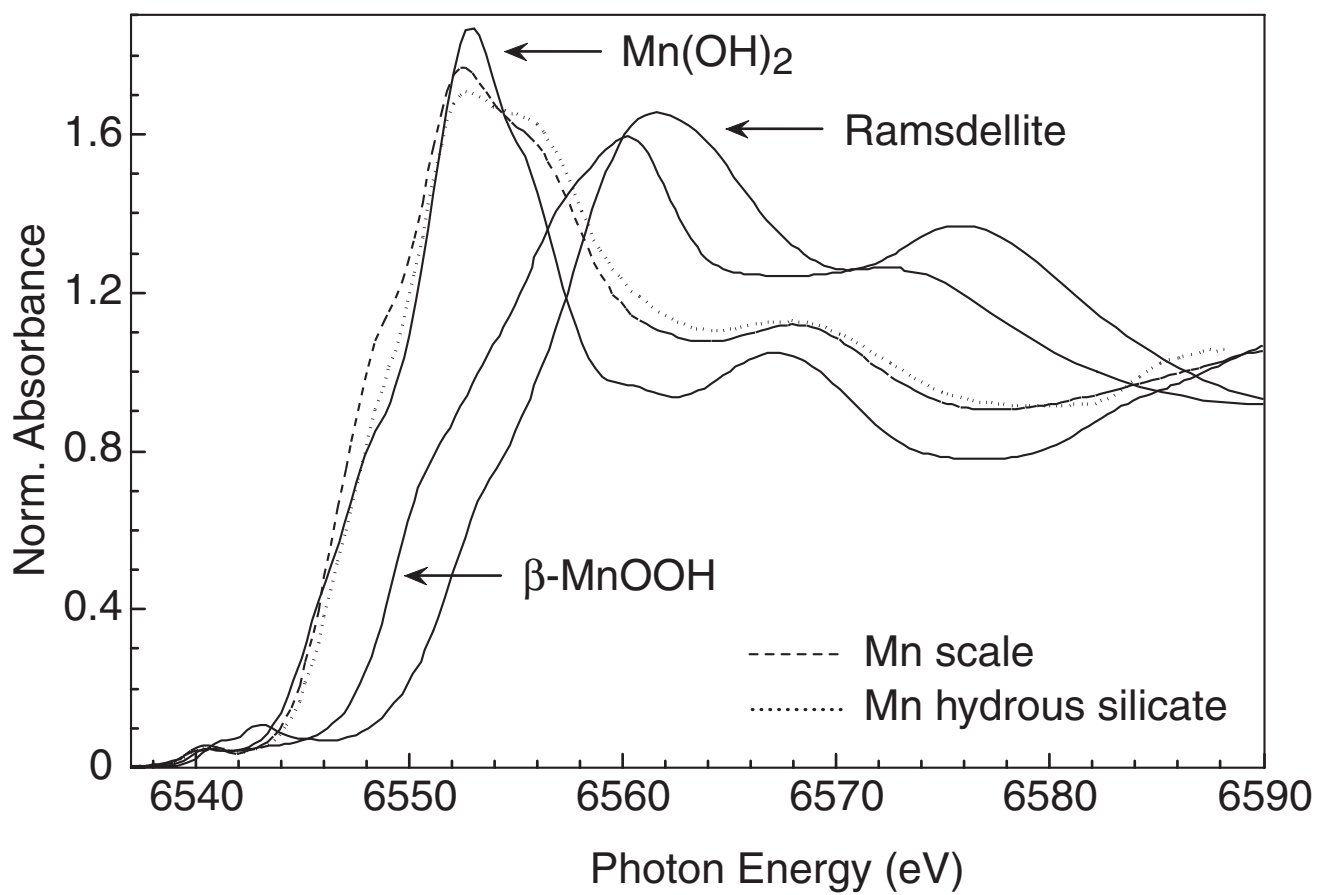


Fig. 3 Manceau and Gallup

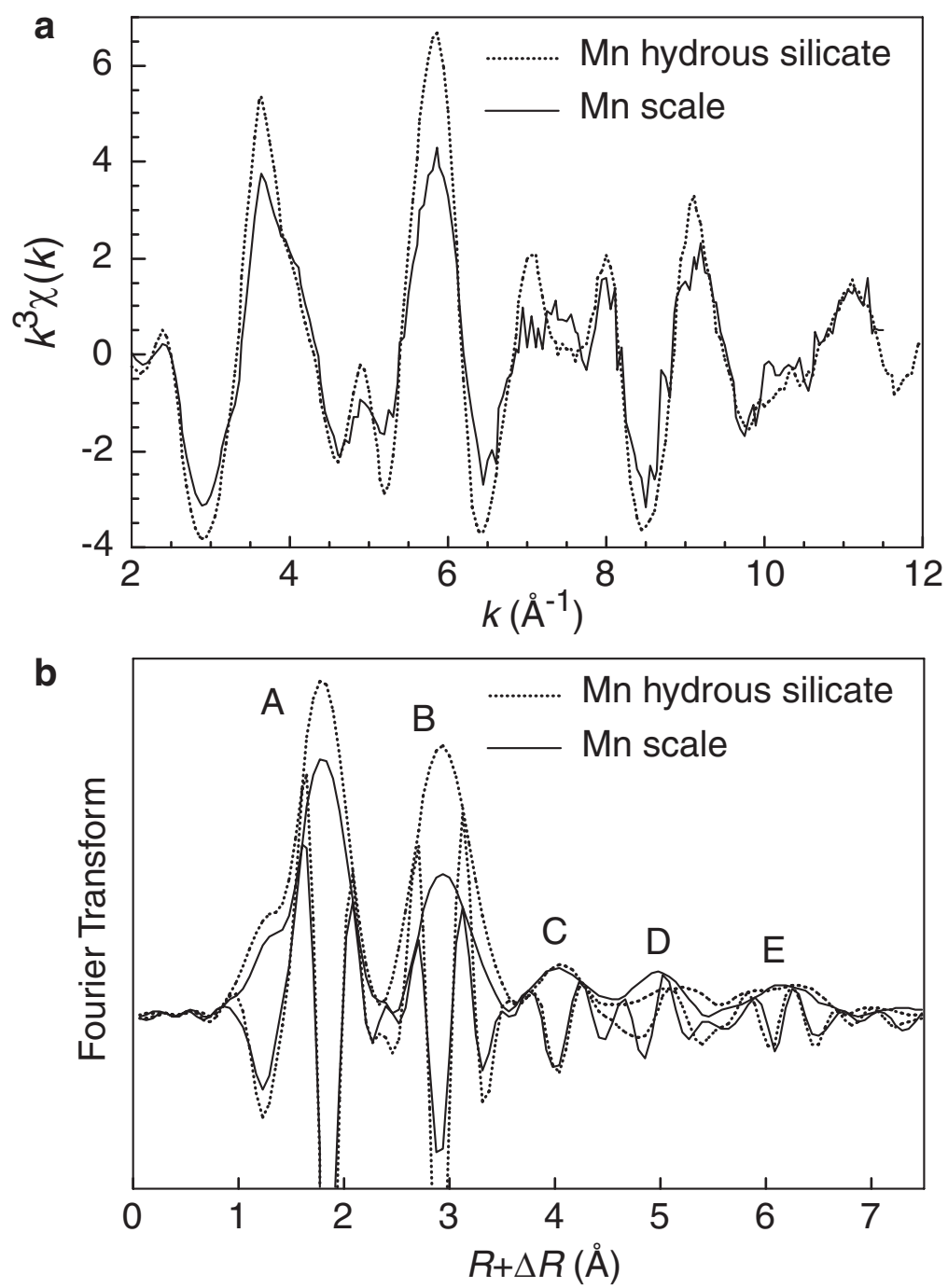


Fig. 4 Manceau and Gallup

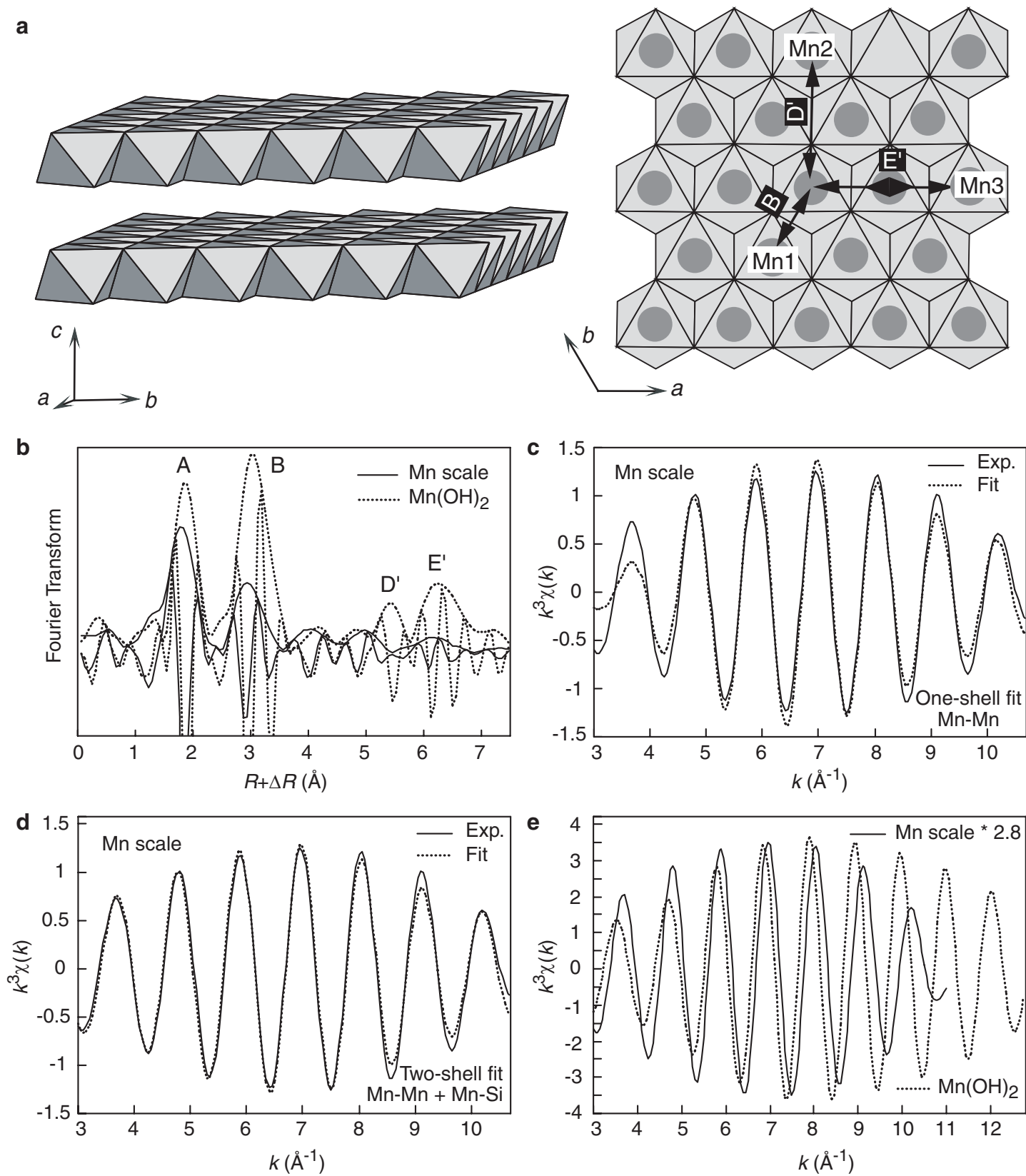


Fig. 5 Manceau and Gallup

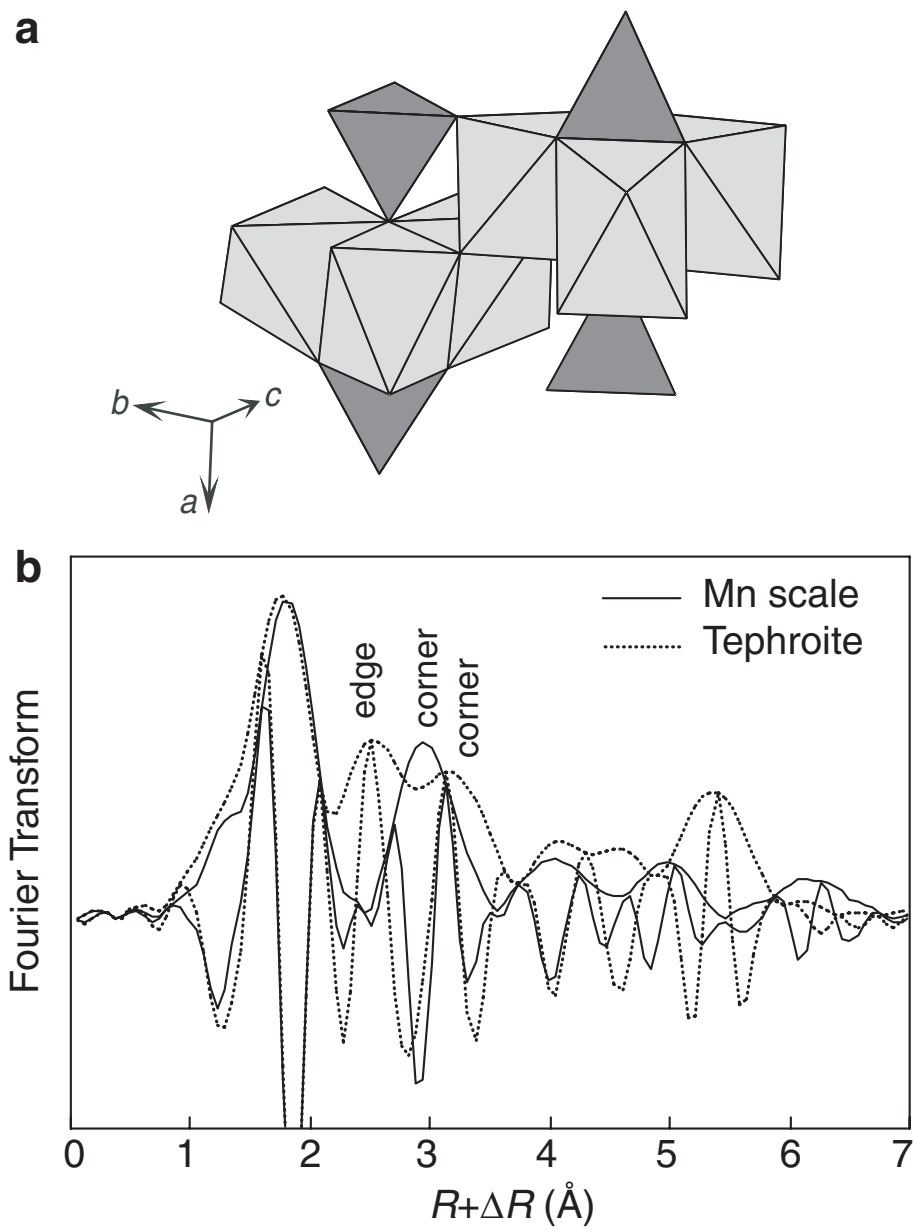


Fig. 6 Manceau and Gallup

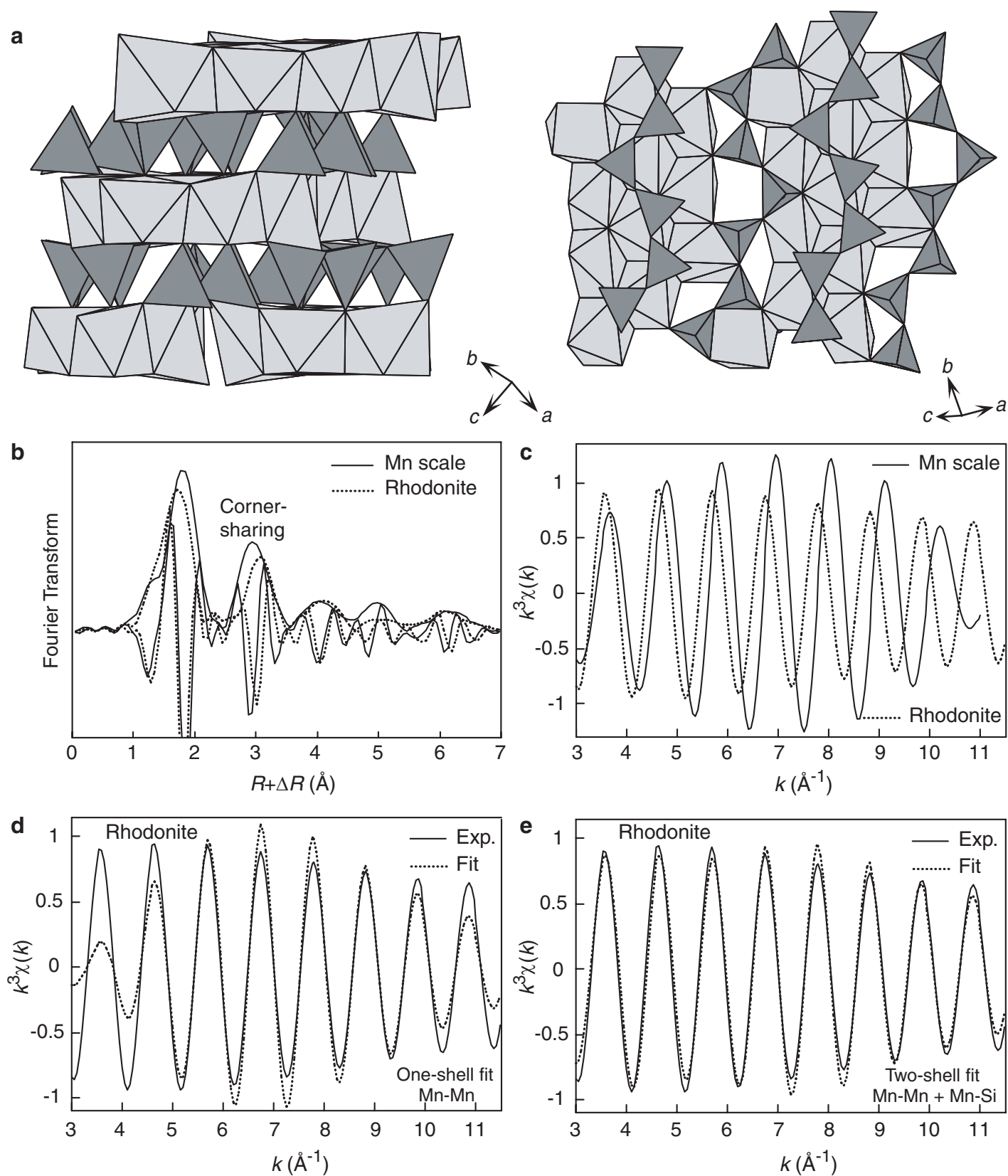


Fig. 7 Manceau and Gallup

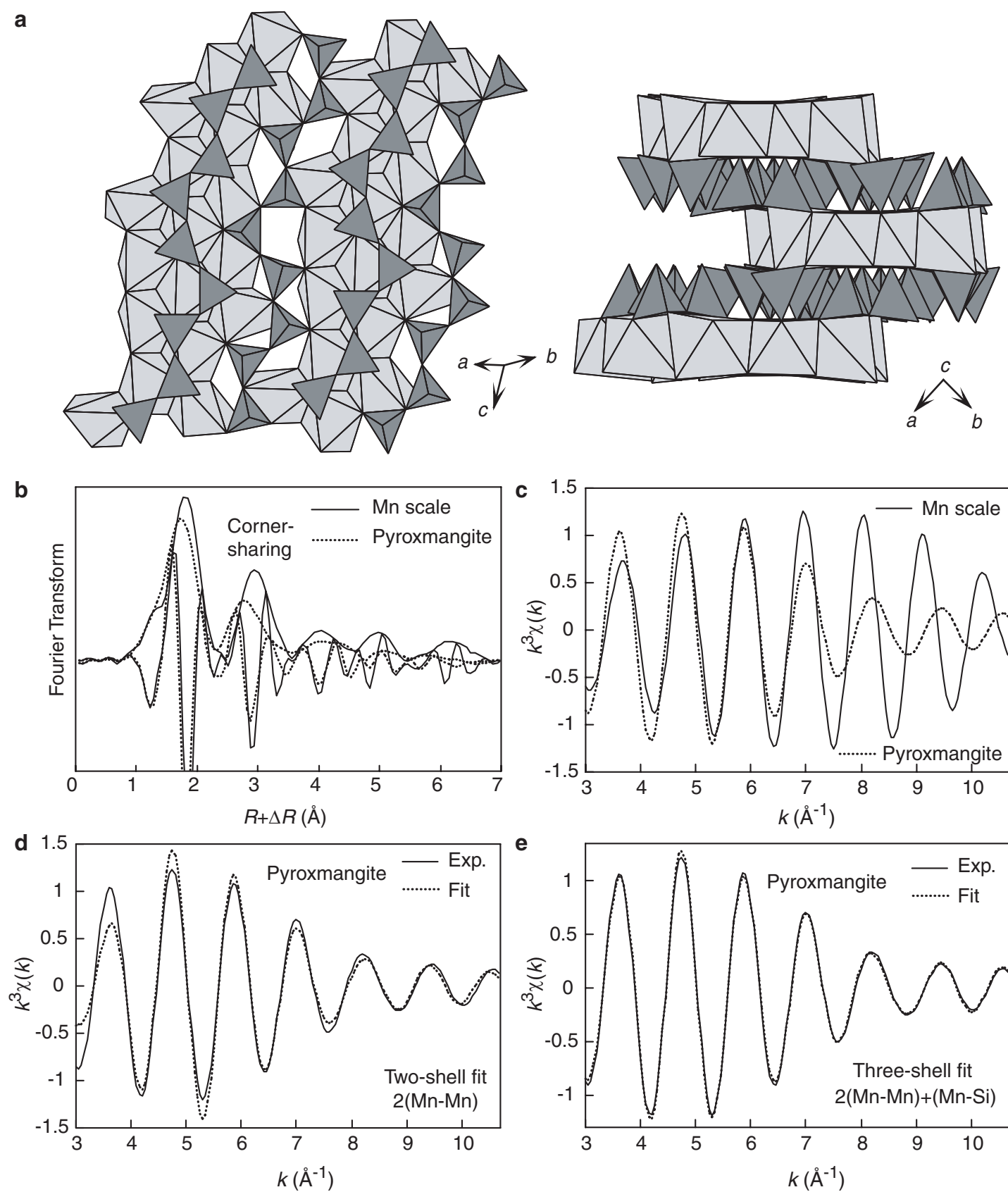


Fig. 8 Manceau and Gallup

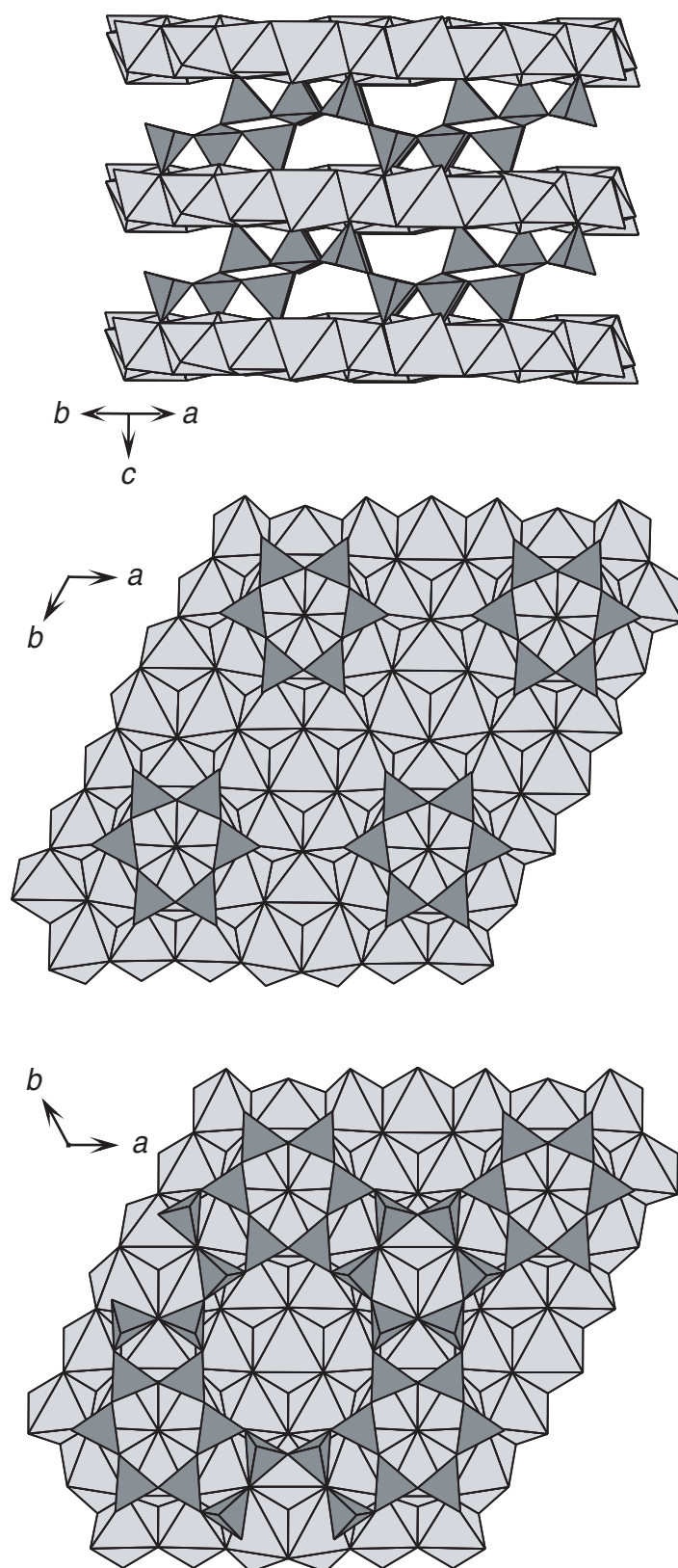


Fig. 9 Manceau and Gallup

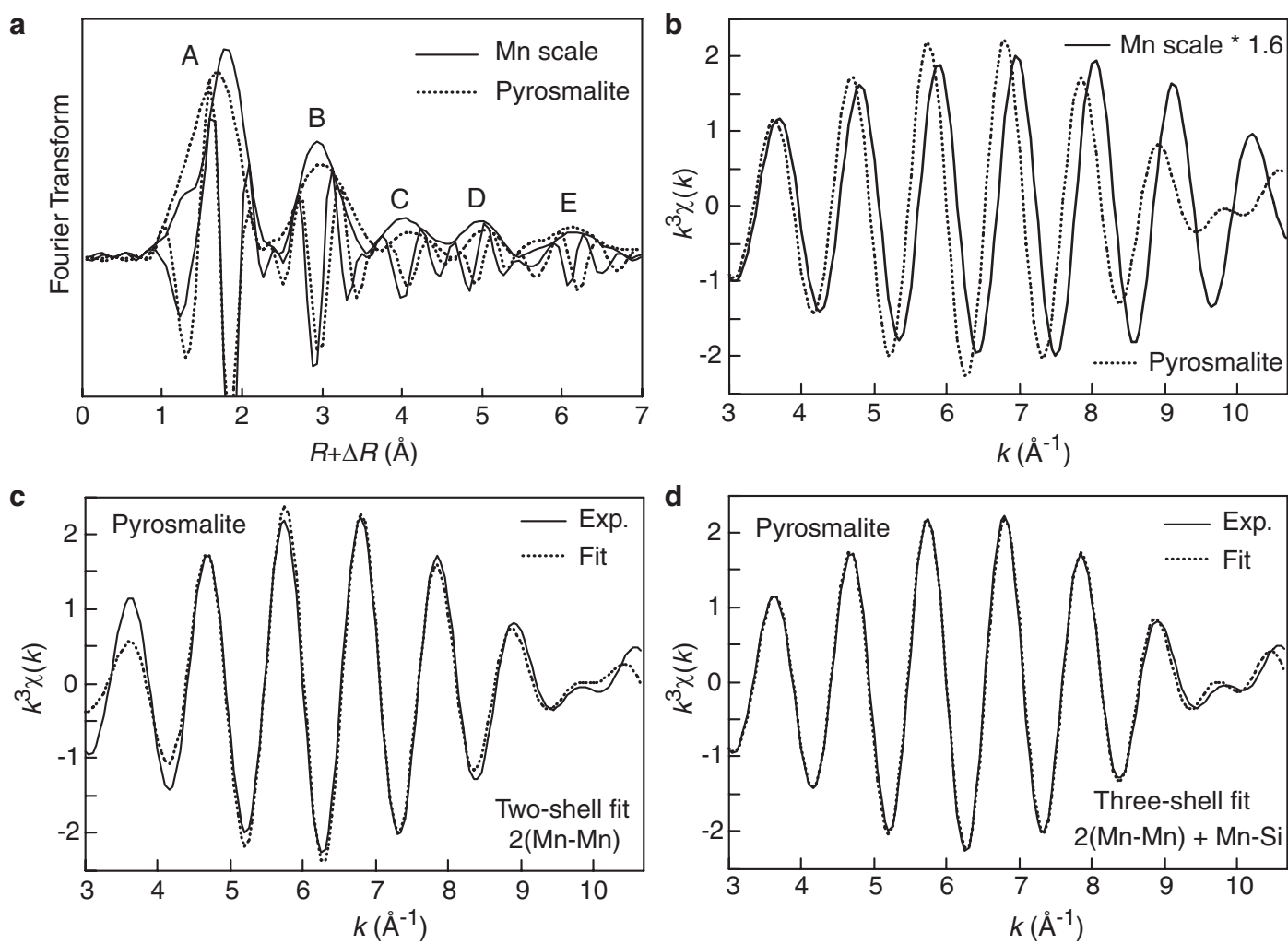


Fig. 10 Manceau and Gallup